
CHICAGO JOURNALS

Multiple-Aperture-Based Solar Seeing Profiler
Author(s): Deqing Ren, Gang Zhao, Xi Zhang, Jiangpei Dou, Rui Chen, Yongtian Zhu, and Feng Yang
Source: *Publications of the Astronomical Society of the Pacific*, Vol. 127, No. 955 (September 2015), pp. 870-879
Published by: The University of Chicago Press on behalf of the Astronomical Society of the Pacific
Stable URL: http://www.jstor.org/stable/10.1086/682746
Accessed: 02/10/2015 17:06

Your use of the JSTOR archive indicates your acceptance of the Terms & Conditions of Use, available at http://www.jstor.org/page/info/about/policies/terms.jsp

JSTOR is a not-for-profit service that helps scholars, researchers, and students discover, use, and build upon a wide range of content in a trusted digital archive. We use information technology and tools to increase productivity and facilitate new forms of scholarship. For more information about JSTOR, please contact support@jstor.org.

The University of Chicago Press and *Astronomical Society of the Pacific* are collaborating with JSTOR to digitize, preserve and extend access to *Publications of the Astronomical Society of the Pacific.*

http://www.jstor.org

This content downloaded from 130.166.194.113 on Fri, 2 Oct 2015 17:06:50 PM
All use subject to JSTOR Terms and Conditions

PUBLICATIONS OF THE ASTRONOMICAL SOCIETY OF THE PACIFIC, **127**:870–879, 2015 September
© 2015. The Astronomical Society of the Pacific. All rights reserved. Printed in U.S.A.

Multiple-Aperture-Based Solar Seeing Profiler

DEQING REN,[1,2,3] GANG ZHAO,[2,3] XI ZHANG,[2,3] JIANGPEI DOU,[2,3] RUI CHEN,[2,3] YONGTIAN ZHU,[2,3] AND FENG YANG[2,3]

Received 2015 February 06; accepted 2015 June 12; published 2015 August 12

ABSTRACT. Characterization of day-time atmospheric turbulence profiles up to 30 km above the telescope is crucial for designs and performance estimations of future solar multiconjugate adaptive optics (MCAO) systems. Recently, the S-DIMM+ method has been successfully used to measure the vertical profile of turbulence. However, to measure profile up to 30 km employing the S-DIMM+ method, a telescope with a diameter of at least 1.0 m is needed, which restricts the usage of S-DIMM+, since large telescopes are scarce and their time is limited. To solve this problem, we introduce the multiple-aperture seeing profiler (MASP), which consists of two portable small telescopes instead of a single large aperture. Numerical simulations are carried out to evaluate the performance of MASP. We find that for one layer case, MASP can retrieve the seeing with error ∼5% using 800 frames of wavefront sensor (WFS) data, which is quite similar to the results of a telescope with diameter of 1120 mm. We also simulate profiles with four turbulence layers, and find that our MASP can effectively retrieve the strengths and heights of the four turbulence layers. Since previous measurements at Big Bear Solar Observatory showed that day-time turbulence profile typically consists of four layers, the MASP we introduced is sufficient for actual seeing measurement.

Online material: color figures

1. INTRODUCTION

Measurements of the profile of the atmospheric optical turbulence as a function of altitude, $C_n^2(h)$, are crucial for the actual performance estimation of any adaptive optics (AO) (Ren et al. 2014; Rousset et al. 2003; Wildi et al. 2003; van Dam et al. 2006; Boccas et al. 2008; Myers et al. 2008), including the solar multiconjugate AO (MCAO) systems that are being developed for future 4-m solar telescope (Berkefeld & Soltau 2010; Rimmele & Marino 2011; Schmidt et al. 2014). Anisoplanatism of the point-spread function for images obtained with AO correction can be characterized if contemporaneous turbulence profile measurements are available (Wilson & Jenkins 1996; Fusco et al. 2000; Britton 2006).

A number of methods have previously been employed to measure the vertical profile of turbulence, including balloon-borne probes (Vernin & Munoz-Tunon 1994), acoustic sounding (Travouillon et al. 2003), and optical methods based on measurements of stellar scintillation including multiaperture scintillation sensor (MASS) (Tokovinin et al. 2003) and scintillation detection and ranging (SCIDAR) (Vernin & Munoz-Tunon 1994; Egner & Masciadri 2007; Avila et al. 2008).

SLOpe Detection And Ranging (SLODAR) is an optical turbulence profiling method based on the use of a Shack–Hartmann wave-front sensor (SHWFS) to observe double star targets (Wilson 2002). In this approach, the seeing profile is retrieved in the frequency domain. Like SCIDAR, SLODAR is an example of a crossed-beams triangulation technique for turbulence sensing. Details of the method for recovery of the turbulence profile from the cross-covariance of the SHWFS data for two stars are described by Butterley et al. (2006). The same approach can be applied to recover the turbulence profile from the cross-correlation of the multiple SHWFS measurements in a tomographic AO system (Tokovinin & Viard 2001; Milton et al. 2007; Wang et al. 2008).

Currently, one of the commonly used techniques for the seeing test is the differential image motion monitor (DIMM), proposed by Sarazin & Roddier (1990). A major advantage for the DIMM is that it uses differential image shift to calculate the overall Fried parameter r_0. Thus, telescope motion and tracking error have no impact on the Fried parameter measurement. This technique was used for ESO site testing and is still widely used for todays site surveys, including those in the Antarctic (Aristidi et al. 2009; Okita et al. 2013). An instrument similar to the DIMM, the S-DIMM (Zhong & Beckers 2001; Beckers 2002) was built for site testing for the Daniel K. Inouye Solar Telescope (DKIST, formerly the Advanced Technology Solar Telescope, ATST), but using one-dimensional differential motion of the solar limb, measured through two 5 cm subapertures.

[1] Physics and Astronomy Department, California State University Northridge, 18111 Nordhoff Street, Northridge, CA 91330; deqing.ren@csun.edu.

[2] National Astronomical Observatories/Nanjing Institute of Astronomical Optics and Technology, Chinese Academy of Sciences, Nanjing 210042, China; gzhao@niaot.ac.cn.

[3] Key Laboratory of Astronomical Optics and Technology, Nanjing Institute of Astronomical Optics and Technology, Chinese Academy of Sciences, Nanjing 210042, China.

This content downloaded from 130.166.194.113 on Fri, 2 Oct 2015 17:06:50 PM
All use subject to JSTOR Terms and Conditions

While the scintillation detection can be used for the night-time seeing profile measurement, it is not suitable for the solar measurement where the target images are two-dimensional extended structures, such as the solar granulation. As a part of the design study for the European Solar Telescope (EST), a program for studying two potential sites, one on La Palma and one on Tenerife, has been initiated. The goal is to characterize the height distribution of contributions to seeing at the two sites and to define requirements for an MCAO system for the EST in good seeing conditions. At present, very little work has been published on characterization of high-altitude seeing based on wave front sensors operating on solar telescopes. Measurements of scintillation of sunlight with a linear array of detectors have been shown to be sensitive to the height distribution of seeing contributions (Seykora 1993; Beckers 1993, 2002). Because of the integration of contributions to scintillation over the large solid angle subtended by the solar disk, an array of detectors with fairly large baseline is needed to achieve sensitivity up to a height of only 500 m (Beckers 1993). Instrumentation that utilizes this technique, referred to as shadow band ranging (SHABAR; Beckers 2001), was built to characterize near ground seeing in connection with site testing for the DKIST (Hill et al. 2006).

To address the problem of solar seeing profile measurement, Scharmer & van Werkhoven (2010) proposed a seeing profiler called S-DIMM+, which is based on SHWFS, and the seeing profile is retrieved in the spatial domain. To achieve good height resolution and high-altitude profile measurement, this method needs to use existing solar telescopes with a large aperture size at least 1.0 m, such as the Big Bear Solar Observatory (BBSO) 1.6-m New Solar Telescope (NST). Recently, Kellerer et al. (2012) used the S-DIMM+ technique and measured the seeing profile at the BBSO, and the measurement was conducted with the 1.6 m NST. The NST-based S-DIMM+ experience yields a turbulence profile measurement of four layers, with the maximum height up to 8 km. This is the only ground-based day-time seeing profile measurement using solar extended structures for the wave-front sensing. In fact, since the SLODAR and the S-DIMM+ use identical hardware, the limitation applied on the SLODAR also applies on the S-DIMM+, which is determined by the physics laws of the SHWFS. To achieve high-angular-resolution imaging in the visible over a field of view (FOV) up to 60″, the next generation MCAO with future 4 m solar telescopes will need to have five deformable mirrors (DMs) (Berkefeld & Soltau 2010). For the design and accurate performance estimation of such a complex MCAO system with a large number of DMs, a discrete turbulence distribution of at least 10 layers is needed. Since high-altitude turbulence has large contribution to the small isoplanatic angle and turbulence may extend to high altitude such as 25 km, turbulence information up to high altitudes of 25 km are also needed. Unfortunately, for the SHWFS hardware, the maximum sample height, which is the maximum vertical height that a SHWFS can measure, is limited by the telescope aperture size used for the seeing profile measurement (Butterley et al. 2006). As a result, both SLODAR and S-DIMM+ need the use of a large telescope. In fact, this limitation also applies to the scintillation-based method (Avila 2012). The need for an existing large telescope is a serious limitation that prevents this technique from being applied on a potential new site where no large telescope currently exists.

Here, we propose a new technique called multiple-aperture seeing profiler (MASP) for day-time solar seeing profile measurement, which will be able to measure the seeing profile up to 30 km. The MASP consists of two small portable telescopes and it will have a large equivalent aperture, and thus can deliver a large maximum sample height. The MASP is a low-cost, portable system, and is especially suitable for a new site-seeing profile measurement where no large solar facility telescope is available. The MASP can be used for the solar seeing profile measurement for the 4 m DKIST, at Maui, Hawaii, which is currently unavailable.

2. CURRENT SHWFS-BASED SEEING PROFILE MEASUREMENTS AND LIMITATIONS

The possibility of using SHWFS observations of binary stars to estimate turbulence profile has been suggested by Welsh (1992) and Bally et al. (1996). The SLODAR (Wilson 2002; Butterley et al. 2006) is a similar method that measures the SHWFS local slopes of two binary stars. Figure 1 shows the generational principle of the SLODAR. It is based on a SHWFS that measures the averaged local wave-front slope of two guide stars across the telescope pupil using an array ($N \times N$) of square subapertures or lenslets. For the SLODAR, the seeing profile is retrieved from the measurement data by using

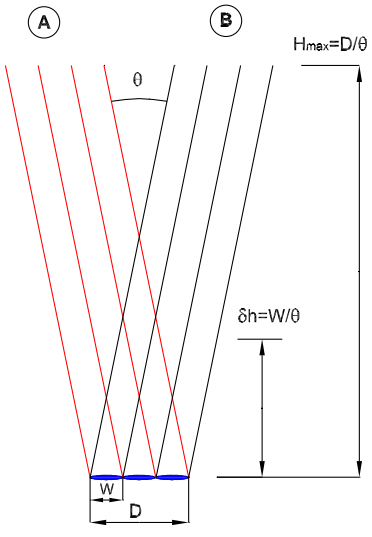

FIG. 1.—Diagram showing the seeing profile measurement with a SHWFS. See the online edition of the *PASP* for a color version of this figure.

This content downloaded from 130.166.194.113 on Fri, 2 Oct 2015 17:06:50 PM
All use subject to JSTOR Terms and Conditions

frequency domain method. Recently, the generalized SLODAR was proposed by Goodwin et al. (2007), which can remove mirror and dome seeing turbulence, and provide a height resolution by a factor of 3. This technique has reached a degree of maturity exhibiting reasonable agreement when used together in campaigns (Tokovinin & Travouillon 2006).

For the seeing profile measurement, the vertical resolution and the maximum sample height are two important parameters. The vertical resolution defined the smallest vertical height that the SHWFS instrument can measured, and it is given by $\delta h = w/\theta$, where w is the SHWFS subaperture size projected on the telescope aperture, and θ is the field angle of the two subfields. The maximum sample height determined the highest layer that the SHWFS and telescope combination can effectively measure and is given as $H_{\max} = D/\theta$, where D is the telescope effective diameter used for the seeing profile measurement. This equation applies to SLODAR, S-DIMM+, and the scintillation methods.

The SLODAR was only used for night-time seeing profile measurement. Current BBSO site tests using the S-DIMM+ technique can only deliver four layers of the turbulence profile with a maximum sample height of 8 km (Kellerer et al. 2012), because of the limited time available for the site test (private communication with Kellerer, 2014). To achieve an accepted performance (Strehl ratio better than 0.2) over the 60″ field of view at the 0.5 μm, future MCAO systems will have up to 5 DMs, conjugated from the ground to a height of 30 km above the telescope (Berkefeld & Soltau 2010). Further increasing the maximum sample height and the measured turbulence layer number are critical for the optimized design as well as the performance estimation of a MCAO system.

It is clear that a portable telescope can only deliver a small maximum sample height, because of the small telescope aperture size. Even though, such a portable telescope is still useful for the measurement of local ground layer seeing profile. A prototype portable SLODAR system was commissioned by ESO for statistical characterization of atmospheric turbulence in relation to the application of AO imaging at the Very Large Telescope (VLT) (Wilson et al. 2004). The instrument was optimized for detailed study of the ground layer of optical turbulence, in approximately the first kilometer above the site. In particular, the aim was to distinguish the turbulence contribution from the surface layer (SL), corresponding to the first 100 m altitude, and the detailed profile of turbulence in the range of altitudes from 100 to 1000 m, referred to as the gray zone (GZ) (Tokovinin 2004). Recently, a portable SLODAR with 400 mm telescope aperture was developed by Durham University (Wilson et al. 2009). Because of the small telescope aperture, this portable system can only achieve a maximum sample height of 2000 m. SODAR (sound detection and ranging) was also used to measure the turbulence profile in the South Pole, limited to a height up to 890 m (Travouillon et al. 2003).

3. PROPOSED SEEING PROFILE MEASUREMENT INSTRUMENT

3.1. The MASP Methodology

For a site-seeing profile measurement, it will be extremely useful if a portable system with a telescope aperture size of $300 \sim 400$ mm can be used for such a purpose. This is mandatory for a new candidate site where no large facility telescope exists. Unfortunately, because of the limit of the small aperture size, current techniques cannot allow a portable system to be used for the seeing profile measurement with enough maximum sample height. In addition, at an existing site with a large telescope such as the 1.6 m NST at the BBSO, the telescope time that can be used for the site-seeing test is very limited. Therefore, it is highly desirable that a portable system can be used for the seeing profile measurement that can only be done currently with a large telescope.

To solve the maximum sample height problem, we propose the MASP, which can provide a large maximum sample height, and at the same time, can also provide good vertical resolution for detail characterization of the turbulence profile at the altitude near the ground layer. Our MASP consists of two small telescopes, each with a size on the order of ~400 mm. The small telescopes are arranged in a linear array to sample the large aperture of a large equivalent telescope. Therefore, they can provide an equivalent aperture size that is equal to the large telescopes aperture. In actual seeing profile measurement, the two small telescopes can point on the same solar structures for wave-front sensing.

3.2. MASP Instrument

Since the SLODAR and S-DIMM+ seeing profiler use a single aperture telescope and a SHWFS to measure the seeing profile, as shown in Figure 1. In such a system, each SHWFS subaperture can measure the profile to the height $\delta h = w/\theta$. While a single subaperture can sample the seeing profile $\delta h = w/\theta$, a single aperture consisting of N linear subapertures can measure the seeing profile up to a height $H_{\max} = Nw/\theta = D/\theta$. Please note that in such a system, only a linear subaperture across the diameter D is used to measure the seeing profile. For such a SHWFS linear array, if we measure from the first subaperture (see Fig. 2*b*), the continuous increase of the subaperture to subaperture distance (or gap) with a step of w implies an increase step of measured seeing profile $\delta h = w/\theta$. Figure 2 shows the comparison of our MASP (Fig. 2*a*) and a class single aperture telescope (Fig. 2*b*) that has an equivalent diameter with our MASP that is almost three times of the small telescope used in our MASP. The useful linear arrays of subapertures of the SHWFS are numbered. In this figure, the MASP consists of two identical small telescopes, each equipped with a SHWFS of five subapertures across the diameter of the small telescope, and the gap between two small telescopes corresponds to four subapertures. The corresponding equivalent single-aperture

This content downloaded from 130.166.194.113 on Fri, 2 Oct 2015 17:06:50 PM
All use subject to JSTOR Terms and Conditions

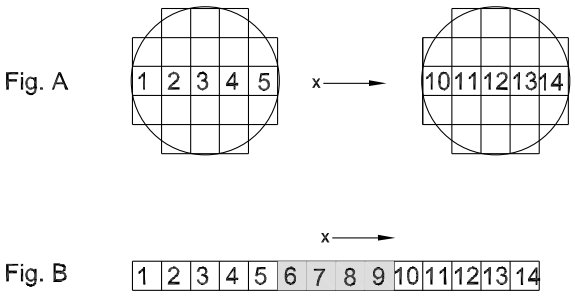

FIG. 2.—SHWFS lenslet layout.

telescope shown in Figure 2*b* has 14 SHWFS subapertures across its diameter. Compared with the large equivalent telescope, the subapertures 6–9 are missed in our MASP, because of the gap between the two small telescopes. If the subaperture distance is measured from the first subaperture (called start subaperture herein, and it is numbered as 1 in this figure) on the left side of the MASP, only the subapertures from the number 1 to number 5, and 10 to number 14, are continuously increased in the subaperture distance with a step w (where w is the subaperture diameter). The numbers 6–9 associated subaperture distances $5w \sim 8w$ are missed as a result of the gap between of the two small telescopes.

However, the missing subapertures-associated distances can be found by changing the start subaperture. It is important to note that in the retrieving process of the seeing profile, the covariance used is a function of the subaperture distance only and it is independent to the subaperture coordinates, which means that we can use any two subapertures of the same distance to measure the seeing profile. If we choose the start subaperture as number 5, it can be combined with subapertures 10–13 and provide the missing subaperture distances. For example, the subaperture 5 and 10 combination will provide a subaperture distance of $5w$, while subaperture 5 and 13 combination will provide a subaperture distance of $8w$. In such an approach, the missing subaperture distances of $6w$ to $8w$ are found. Furthermore, for each distance, we may find more than one pairs of subapertures. For example, three combinations of subapertures (3–10, 4–11, and 5–12) have distance of $7w$. In Figure 3, we plot the number of subaperture combinations versus the subaperture distance. The black solid line plot the case of MASP with the pupil distance of $4w$. We can see that at least one combination of subapertures can be found for distance from $1w$ to $13w$, which indicates that our MASP, consisting of two 400 mm diameter small telescopes, is equivalent to an 1120 mm diameter telescope for the seeing profile measurement. If the pupil distance is decreased to $3w$ (blue dash-dotted line in Fig. 3), the effective diameter is decreased to 960 mm. If pupil distance is set to be $5w$ (red dashed line), although the effective diameter is increased to 1200 mm, no subaperture pair has a distance of $5w$. This is the reason why the pupil distance is set as $4w$ in the MASP.

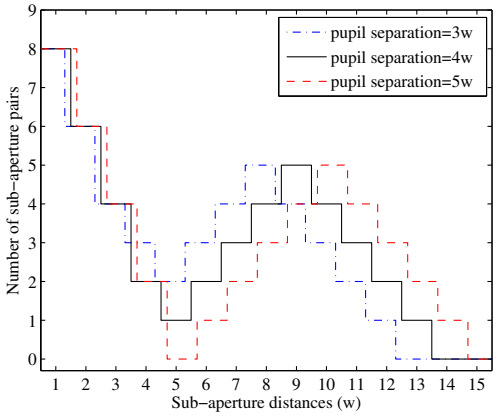

FIG. 3.—Number of subaperture combination vs. the subaperture distance. See the online edition of the *PASP* for a color version of this figure.

Table 1 lists our MASP major specifications. Each subaperture has a $91'' \times 91''$ field of view (FOV). The SHWFS subaperture projected onto the telescope aperture is equal to 80 mm in diameter, which corresponds to an angular resolution of $1.3''$ at the 0.5 m wavelength. Such a large subaperture size is needed to resolve the solar granules, which has a typical size between $2.0'' \sim 3.0''$. The MASP uses two small subfields on the solar surface as guide stars for the seeing profile measurement, and a small granulation region with a size of $\sim 5'' \times 5''$ can be used as a guide star. The separation of the two subfields can be chosen between $8''$ and $58''$. In the case that the two subfields have a separation of $8''$ and the MASP has a 1120 mm equivalent diameter, our MASP can provide a maximum sample height of 29 km and a vertical resolution of 2050 m, while with the $58''$ separation, it delivers a smallest vertical resolution of 280 mm and a maximum sample height of 4 km.

3.3. Seeing Profile Retrieving

In principle, both seeing profile retrieving algorithms with the SLODAR and S-DIMM+ can be used for our MASP. The S-DIMM+ algorithm is inherent from the DIMM originally proposed by Sarazin & Roddier (1990). A unique feature of the DIMM technique is that it uses the differential image data to calculate the seeing parameter. Therefore, the impact from the telescope vibration and tracking error is eliminated. In

TABLE 1
MASP SPECIFICATIONS

Equivalent diameter	1120 mm
Working wavelengths	500 μm
Small-telescope diameter	400 mm
Subfield separation	$58''/8''$
Subaperture diameter	80 mm
Vertical resolution	280/2050 m
Maximum sample height	4/29 km

This content downloaded from 130.166.194.113 on Fri, 2 Oct 2015 17:06:50 PM
All use subject to JSTOR Terms and Conditions

addition, the S-DIMM+ is relatively simple to implement and thus is used for our MASP.

Assume that the relative image displacements are either along (longitudinal or x component) or perpendicular (transverse or y components) to the line connecting the centers of two subapertures. Again, assume that one of the subapertures is located on the original, and the second subaperture is located a distance s from the first subaperture. The field angle of the first subfield is assumed to be zero, while the second subfield is θ with the measurement telescope. For N layers of atmospheric turbulence, the first measurement δx_1 is the added contributions of each layer located at height h_n

$$\delta x_1(s,0) = \sum_{n=1}^{N}[x_n(s) - x_n(0)]. \tag{1}$$

For the second measurement, δx_2

$$\delta x_2(s,\theta) = \sum_{n=1}^{N}[x_n(s+\theta h_n) - x_n(\theta h_n)]. \tag{2}$$

The covariance between δ_1 and δ_2 is defined as

$$\langle \delta x_1 \delta x_2 \rangle = \sum_{n=1}^{N} \langle [x_n(s) - x_n(0)][x_n(s+\theta h_n) - x_n(\theta h_n)] \rangle, \tag{3}$$

where $\langle \ldots \rangle$ represents average over a large number of short exposure images. As demonstrated by Scharmer & van Werkhoven (2010), equation (3) can be eventually calculated as

$$\langle \delta x_1 \delta x_2 \rangle = \sum_{n=1}^{N} c_n F_x(s,\theta,h_n), \tag{4}$$

and similarly, in the y direction we have

$$\langle \delta y_1 \delta y_2 \rangle = \sum_{n=1}^{N} c_n F_y(s,\theta,h_n), \tag{5}$$

where

$$\begin{aligned} F_x(s,\theta,h_n) = {} & I((\theta h_n - s)/D_{\text{eff}}, 0)/2 \\ & + I((\theta h_n + s)/D_{\text{eff}}, 0)/2 - I((\theta h_n)/D_{\text{eff}}, 0), \end{aligned} \tag{6}$$

$$\begin{aligned} F_y(s,\theta,h_n) = {} & I((\theta h_n - s)/D_{\text{eff}}, \pi/2)/2 \\ & + I((\theta h_n + s)/D_{\text{eff}}, \pi/2)/2 \\ & - I((\theta h_n)/D_{\text{eff}}, \pi/2). \end{aligned} \tag{7}$$

The coefficient c_n is expressed in each layer and is related the Fried parameter of that layer as

$$c_n = 0.358\lambda^2 r_0(h_n)^{-5/3} D_{\text{eff}}^{-1/3}. \tag{8}$$

For square subaperture, according to Kellerer (2015), the functions $I(z,0)$ and $I(z,\pi/2)$ are defined as

$$I(z,0) = 2 - |1-z|^{5/3} + 2|z|^{5/3} - |1+z|^{5/3}, \tag{9}$$

$$I(z,\pi/2) = 2 + 2|z|^{5/3} - 2(1+z^2)^{5/6}. \tag{10}$$

The efficient diameter D_{eff} is the maximum of D. Be noted that the above equations can be used to the two subapertures with a closed distance, including $s/D < 1$ and s/D as large as 50.

The left sides of equations (4) and (5) are the measurement data of the SHWFS of any two subapertures. In each direction (x or y), we can list at least 26 equations, which can be used to retrieve the unknown parameters $(r_0(h_1), \ldots, r_0(h_i), \ldots, r_0(h_n))$ located at the corresponding height h_i, respectively. More equations can be listed if combinations from other rows are included. The large redundant equations can be used to retrieve the local Fried parameter $r_0(h_i)$ up to ~10 layers. The local seeing parameter $C_n^2(h_n)$ is related to the local Fried parameter $r_0(h_n)$ as

$$r_0 = \left[0.423\left(\frac{2\pi}{\lambda}\right)^2 (\cos\phi)^{-1} C_n^2(h) dh\right]^{-3/5}, \tag{11}$$

where λ is the wavelength and ϕ is the zenith angle. The above equation can also be used to calculate the over Fried parameter r_0 as

$$r_0 = \left[0.423\left(\frac{2\pi}{\lambda}\right)^2 (\cos\phi)^{-1} \int C_n^2(h) dh\right]^{-3/5}. \tag{12}$$

4. NUMERICAL SIMULATION

In order to test the idea of the MASP as well as evaluate its performance, we employ a Monte Carlo numerical simulation to study the seeing retrieving process. The simulation code is written in Interactive Data Language (IDL). In the following, we detail the steps of the simulation.

1. Kolmogorov phase screen is generated for each layer of atmosphere according to Johansson & Gavel (1994). The Fried parameter r_0 of each layer is set to be 0.1, and outer scale L_0 is set to be infinity. In our simulation, we use 16 pixels to sample the 80 mm subaperture, which means the pixels size on the phase screens is 5 mm pixel^{-1}. The size of the phase screen is set as $k \times (D + h \times \text{FOV})$, which has different sizes to accommodate the FOV at different heights and k is a enlarge factor to avoid the edge effect.

This content downloaded from 130.166.194.113 on Fri, 2 Oct 2015 17:06:50 PM
All use subject to JSTOR Terms and Conditions

2. Two guide stars are generated, which are the approximations of two small region of the solar surface. The simplification will make the simulation faster and simpler. However, the effect of divergence of the beams with height and cross-correlation error of extended targets cant be studied. In our study, we focus on the problem due to multisubaperture, thus using point targets instead of extended targets is acceptable. The separation between the guide stars can be changed from $8''$–$64''$.

3. The phase along the direction of each guide star is computed.

4. The shifts of the guide stars in each subaperture are calculated according to the mean slope of the phase. These shifts values reflect the image displacement at different field angle.

5. New phase screen is generated and steps 1–4 are repeated. In our simulation, the time-interval between two consecutive exposures is assumed longer than the coherence time of daytime turbulence, thus the phase screens are not correlated.

For our MASP configuration descripted in § 3.2, although only subapertures 1–5 and 10–14 are used, subaperture distances from $1w$ to $13w$ can be calculated (see Figs. 2 and 3). Using the relative image displacements, left side of equations (4) and (5), namely, $\langle \delta x_1 \delta x_2 \rangle$ and $\langle \delta y_1 \delta y_2 \rangle$, can be calculated, and we will have 26 equations in total. Thus up to 26 layers of atmosphere can be solved from the equations. Because the r_0 value of each layer cannot be negative, we use the *MATLAB lsqnonneg* function to solving the nonnegative least-squares constraints problem and find the r_0 value of each layer.

4.1. Compare MASP and Single-Aperture Telescope

Since the maximum height is limited by $H_{\max} = D/\theta$, a portable single-aperture telescope with 0.4 m diameter cannot reliably provide a maximum height seeing profile up to 30 km. To achieve such a goal, we need to use the MASP, in which two portable telescopes, each with 0.4 m diameter, are used. In order to test the idea of multiapertures, we compare the performance of our MASP with seeing-profilers using single apertures. We study three cases: (1) MASP, (2) seeing-profiler with aperture of 1120 mm, which is same as the effective diameter of the MASP, and (3) the one with diameter of 400 mm, which is same as the aperture size of an individual telescope in MASP. In the simulations, only one layer of atmosphere with $r_0 = 0.1$ m is considered and its height is changed from 0 to 30 km. The configuration of the subaperture of MASP SHWFS is according to the description of § 3.2. For all the three cases, the size of subaperture of SHWFS is 80 mm, and the field angle separation of the two subfields is $8''$. In total, 800 set of shifts values are used in each case. In the seeing–retrieving process, we assume that the height of the layer is already known, namely, we will not find the height of the layer. In Figures 4*a*–4*c*, the results of MASP, 1120 mm apertures and 400 mm apertures are shown, respectively. The black solid lines with squares show the estimated r_0 for different height of atmosphere layer. Since the atmospheric turbulence phase is randomly changed, statistical error will exist in the r_0 estimation. In order to find this error, we repeat the simulation, estimate 14 groups of r_0, and calculate the rms values. The error bars in the figure indicate the 1-σ error. The dashed line indicates the input value of $r_0 = 0.1$ m, and the vertical dotted line represents the limited maximum height $H_{\max} = D/\theta$. In Figure 4*a*, the results of MASP are plotted. As shown in Table 1, the MASP has an equivalent diameter of 1120 mm. Since the field angle separation is $8''$, it can measure a maximum height of 29 km with a vertical resolution of 2050 m. We can see in the figure that r_0 can be well estimated within the limited maximum height 29 km. The errors roughly increase with the increase of the height of the layer. For the layer lower than 15 km, the error of r_0 estimation is about 3%; it is about 5% for the layers higher than 15 km, and ~15% for the layer at 30 km. Comparing with Figure 4*b* for a single 1120 mm telescope, we can see our MASP has very similar detection accuracy and maximum height as a big single-aperture telescope, except that the error is slightly smaller (~4%) in the single-aperture case. It can be seen in Figure 3 that we have few available subaperture pairs with separation ~$5w$ due to the configuration of MASP. Thus the precision of seeing estimations using MASP is slightly lower than that of a single aperture. For the 400 mm aperture case, we can see that estimated r_0 for the layer lower

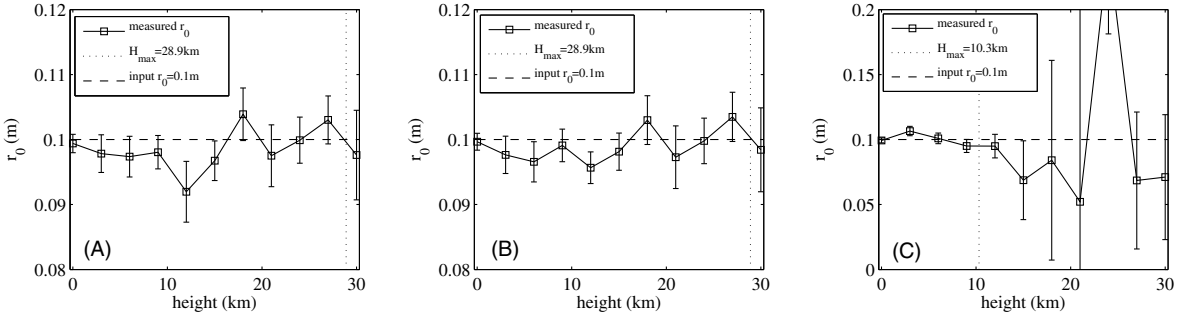

FIG. 4.—Simulation results of seeing profile retrieving for MASP (*a*), 1120 mm aperture (*b*), and 400 mm aperture (*c*), with the estimated r_0 for different height of atmosphere layer (*black solid lines*) and the input r_0 (*dashed lines*).

This content downloaded from 130.166.194.113 on Fri, 2 Oct 2015 17:06:50 PM
All use subject to JSTOR Terms and Conditions

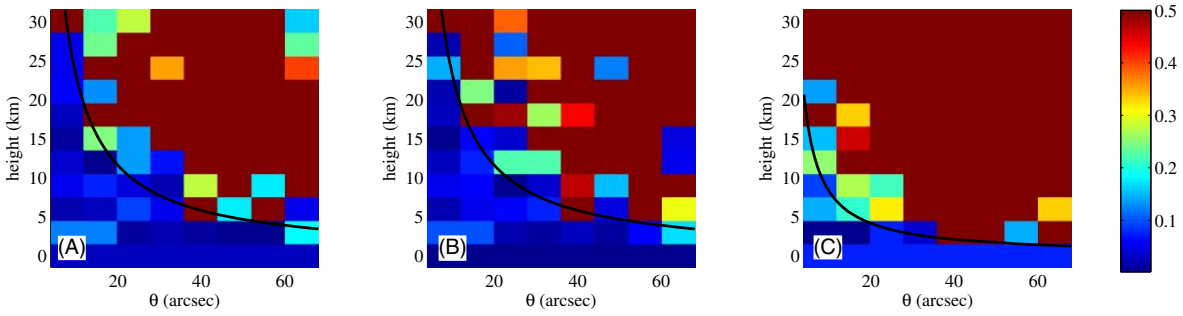

FIG. 5.—Estimated r_0 for different height of atmosphere layer and different field angle separation for MASP (*a*), 1120 mm aperture (*b*), and 400 mm aperture (*c*). The background colors indicate the relative difference between the estimated value and input value. The *black solid lines* show the analytic limited maximum height $H_{\max} = D_{\text{eff}}/\theta$. See the online edition of the *PASP* for a color version of this figure.

than 10 km is in good agreement with the input value, while they do not agree well each other at layer higher than the limited maximum height, as we expected. We noted that the retrieved accuracy can be further improved by using more images (i.e., more than 800 images) in the simulations.

In order to verify the maximum limited height clearly, we change the separation of targets from 8″ to 64″, and investigate how the separation of targets affects the maximum limited height. We change both of the height of layer and separation of the targets in the simulations. For each height and separation, 200 frames of WFS data are simulated. In the seeing–retrieving process, we also assume that the heights of the layers are already known. Figures 5*a*–5*c* plot the results of MASP, 1120 mm aperture, and 400 mm aperture, respectively. The background colors indicate the relative difference between the estimated r_0 and input value. The black solid lines plot the theoretical values $H_{\max} = D/\theta$. When we increase the separation of the two subfields, the maximum height reduces, which agree with the results of numerical simulations for all the three cases. In the MASP case, the results are similar to those of 1120 mm aperture case, which proves that the effective diameter of our MASP is indeed 1120 mm.

4.2. Four-Layer Case

In all of the above simulations, we assume that the layer heights are known in advance, aiming to compare the MASP with single aperture and study the limited maxima height. However, in reality, we do not know the turbulence layer number and the height of each layer. In this case, we can use multiple layers to sample the turbulence profile. We simulate two 2-input atmospheric turbulence models; each contains four turbulent layers, since recently the seeing-profile measurement at BBSO indicated that the day-time turbulence profile distributes in four layers (Kellerer et al. 2012). The parameters of the two profiles are shown in Table 2. Both cases have total $r_0 = 0.1$ m. Profile 1 represents the case with relatively larger isoplanatic angle and is favorable for AO, while Profile 2 has smaller isoplanatic angle, with a much larger contribution for high altitude layers. For each profile, 10,800 short-exposure images are used and 11 layers are used to sample the profile. Among the 11 layers, 10 layers are located from 0 km to 10 km, each with 3 km height separation and one layer is located at 1.5 km. Figure 6 shows the retrieved results. In Figure 6*a*, the fractional $C_n^2(h)$ of each layer are plotted. The black dashed line shows the results of Profile 1, while blue solid line indicates the results of Profile 2. From the figure, we can clearly see four layers located at 0 km, 3 km, 9 km, and 18 km for Profile 1, and 0 km, 6 km, 12 km, and 21 km for Profile 2. Figure 6*b* plots the continuously distributed turbulence of the two profiles. The solid lines are the input profiles, and the dashed lines indicate our retrieved profile. All four layers in each profile are clearly resolved. For Profile 1, the total Fried parameter r_0 is estimated as 0.099 m, which is 1% different from the input value. The r_0 values for each layer are 0.145 m, 0.266 m, 0.315 m, and 0.403 m, which are quite close to the input value, with ~1% relative difference. For Profile 2, the total r_0 we found is 0.101 m, which also has a 1% difference. The r_0 values for each layer are 0.193 m, 0.204 m, 0.278 m, and 0.322 m, with relative differences of 1%, 1%, 6%, and 3%, respectively. It can be seen that the results of Profile 2 have less accuracy. The reason is that the layers in Profile 2 have higher altitude, and we have shown in the last section that the errors roughly increase with the increase of the height of the layer.

For our MASP, the two small telescopes can be installed on a common rigid mount. This approach, of course, requires a

TABLE 2
INPUT SEEING PROFILE

	Layer	Strength of layers	r_0 (m)	Altitude (km)
Profile 1	1	0.55	0.143	0
	2	0.20	0.262	3
	3	0.15	0.312	9
	4	0.10	0.398	18
Profile 2	1	0.35	0.188	0
	2	0.30	0.206	6
	3	0.20	0.263	12
	4	0.15	0.312	21

This content downloaded from 130.166.194.113 on Fri, 2 Oct 2015 17:06:50 PM
All use subject to JSTOR Terms and Conditions

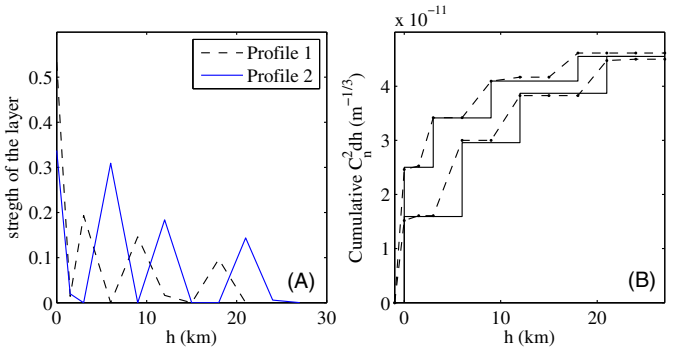

FIG. 6.—Results for the four-layer case. (*a*) Fractional $C_n^2(h)$ of each layer, showing results of Profile 1 (*black dashed line*) and Profile 2 (*blue solid line*). (*b*) Continuously distributed turbulence of the two profiles, showing input profiles (*solid lines*), and the our retrieved profile (*dashed lines*). See the online edition of the *PASP* for a color version of this figure.

dedicated mount to hold the two telescopes as an integrated unit during the seeing measurement. The mount can be located on a large tripod, which can track the sun manually or automatically. The two small telescopes can be purchased from the commercial market as off-the-shelf products.

5. USING TWO INDIVIDUAL TELESCOPES

For our MASP, the two telescopes, each with its individual tripod, can also be used. This allows the use of fully commercialized and computerized telescopes. The two telescopes can point on the same part of the solar granule surface structure. For this approach, we modified equations (4) and (5) for the case with guiding errors.

In our seeing measurement, the relative displacement of the same target observed through different subapertures $\delta x(s,\alpha)$ is measured, where s is the distance of the two subapertures and α is the field angle of the target. If $s \le 4w$, namely, the two subapertures are located at same telescope, a guiding error is not present in the differential image displacement $\delta x(s,\alpha)$, which is the main advantage of DIMM. However, if the two subapertures are located at different telescopes, the measured quantity

$$\delta x(s,\alpha) = \delta\tilde{x}(s,\alpha) + \sigma, \tag{13}$$

where $\tilde{x}(s,\alpha)$ is the term caused by atmospheric turbulence and σ is the displacement between the two telescopes in each short exposure due to the guiding error or vibration in each telescope. For individual exposures, the orientations of the telescopes are fixed, and σ is also a fixed value for each field direction. Thus the different value between $\delta x_1(s,0)$ and $\delta x_1(s,\alpha)$ will not contain a differential orientation error anymore.

$$\langle(\delta x_1 - \delta x_2)^2\rangle = \langle(\delta\tilde{x}_1 - \delta\tilde{x}_2)^2\rangle. \tag{14}$$

Expend both sides, we obtain

$$\langle\delta x_1\delta x_2\rangle = \langle\delta\tilde{x}_1\delta\tilde{x}_2\rangle - \langle\delta\tilde{x}_1^2\rangle/2 - \langle\delta\tilde{x}_2^2\rangle/2 + \langle\delta x_1^2\rangle/2 + \langle\delta x_2^2\rangle/2. \tag{15}$$

According to equation (4) (also eq. [9] in Scharmer & van Werkhoven [2010]), we have

$$\langle\delta\tilde{x}_1\delta\tilde{x}_2\rangle = \sum_{n=1}^{N} c_n F_x(s,\theta,h_n), \tag{16}$$

and

$$\langle\delta\tilde{x}_1^2\rangle = \langle\delta\tilde{x}_2^2\rangle = \sum_{n=1}^{N} c_n F_x(s,0,h_n), = \sum_{n=1}^{N} c_n I(s/D_{\rm eff},0). \tag{17}$$

Substituting equations (16) and (17) into equation (15), we get

$$\langle\delta x_1\delta x_2\rangle = \sum_{n=1}^{N} c_n F_x(s,\theta,h_n) + \Delta_x, \tag{18}$$

where an external term $\Delta_x = \langle\delta x_1^2\rangle/2 + \langle\delta x_2^2\rangle/2 - \sum c_n I(s/D_{\rm eff},0)$ is introduced to correct the guiding error. If the two subapertures are located in the same telescope $\Delta_x = 0$, combining the cases for $s \le 4w$ and $s > 5w$, we obtain the modified equations for the MASP

$$\langle\delta x_1\delta x_2\rangle = \begin{cases} \sum_{n=1}^{N} c_n F_x(s,\theta,h_n), & \text{for } s \le 4w \\ \sum_{n=1}^{N} c_n F_x(s,\theta,h_n) + \Delta_x. & \text{for } s > 4w \end{cases} \tag{19}$$

Similarly, for the y-direction, we also have

$$\langle\delta y_1\delta y_2\rangle = \begin{cases} \sum_{n=1}^{N} c_n F_y(s,\theta,h_n), & \text{for } s \le 4w \\ \sum_{n=1}^{N} c_n F_y(s,\theta,h_n) + \Delta_y. & \text{for } s > 4w \end{cases} \tag{20}$$

where $\Delta_y = \langle\delta y_1^2\rangle/2 + \langle\delta y_2^2\rangle/2 - \sum c_n I(s/D_{\rm eff},\pi/2)$.

In order to test the new equations, we repeat the simulations in § 4.2. Two input atmospheric turbulence models, each contains four turbulent layers are studied. The parameters of the two profiles are shown in Table 2. Similar to the simulation in § 4.2, both cases have total $r_0 = 0.1$ m, and 10,800 short-exposure images are simulated. For each exposure, two random numbers are generated to simulate the orientation errors of the two telescopes, and then they are added to the shift values of images observed by the first and the second telescope, respectively. We arbitrarily assume the guiding errors of the two telescopes are both 10″. Simulations indicate that the guiding errors will not impact the seeing retrieving results if the modified equations are used. Figure 7 shows the results, in which we can see that all of the four layers in each profile are clearly resolved. For Profile

This content downloaded from 130.166.194.113 on Fri, 2 Oct 2015 17:06:50 PM
All use subject to JSTOR Terms and Conditions

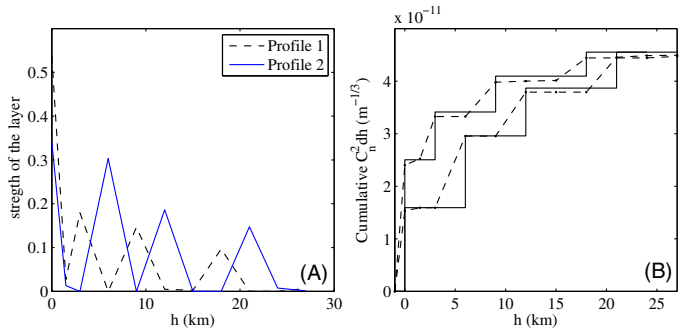

FIG. 7.—Results for the four-layer case, similar to Fig. 6, but with random guiding errors. (*a*) Fractional $C_n^2(h)$ of each layer, showing results of Profile 1 (*black dashed line*) and Profile 2 (*blue solid line*). (*b*) Continuously distributed turbulence of the two profiles, showing input profiles (*solid lines*), and the our retrieved profile (*dashed lines*). See the online edition of the *PASP* for a color version of this figure.

1, the total Fried parameter r_0 we retrieved is 0.101 m, which is 1% different from the input value. The r_0 values for each layer are 0.147 m, 0.283 m, 0.320 m, and 0.411 m, which are quite close to the input value, with 2%, 7%, 3%, and 3% relative difference. For Profile 2, the total r_0 we found is 0.101 m, which also has 1% difference. r_0 values for each layer are 0.192 m, 0.206 m, 0.276 m, and 0.318 m, with relative differences of 2%, 0.1%, 5%, and 2%, respectively. The results show that the problem of orientation errors of individual telescopes is not an obstacle in our MASP.

6. DISCUSSION

In our simulations, we retrieved the seeing profile up to four layers. A total of 26 equations are used to retrieve the seeing, which provides enough precision. When the layer number increases, more equations will be needed to ensure enough redundancy for accurate retrieving. Redundancy can be increased in several ways: based on subapertures 1–5 and 10–14, one can lists more equations for the subaperture pairs with both same and different separations; one can use all 42 subapertures as shown in Figure 2*a*, which will provide more redundant equations; one can repeatedly use the two subfields of same separation, but located at different position in the SHWFS field of view. This guide-star-shift approach, combined with a large SHWFS field of view, provides almost unlimited redundancy for seeing retrieving of multiple layers. Finally, to keep a good precision, one can also use more short-exposure images.

We use the S-DIMM+ method (Scharmer & van Werkhoven 2010) to retrieve the seeing profile. In this method, two small ranges of the solar surface (for example $5'' \times 5''$ for each) are used as two guide stars. However, since we are observing the solar surface, we can select several regions to do the seeing retrieving. In our paper, we mainly discussed the case that the two subfields have field angle separation of 8″. This will provide enough detecting height (29 km), but not good enough vertical resolution (2050 m). If we use another two subfields that have separation of 16″, we can have 1000 m vertical resolution within 15 km. The guide-region pairs with large separation will provide better vertical resolution in lower height, which has strong turbulence and is more important for the AO system. In the extreme situation when the two regions separation equals 0, the S-DIMM+ method is identical to the classic DIMM, and will provide accurate results on the overall r_0. If multiple subfields are used, the layer grid for retrieving the seeing-profile needs to be modified. For example, if three subfields with separation of 8″ and 16″ are used, vertical resolution within 15 km is 1 km, while it is 2 km between 15 and 30 km. Thus, it is more reasonable to use layer grid compact at lower altitude and sparing at higher altitude.

For seeing measurement using an extended target (Sun or Moon), a difficulty is that the effective sensor elements expand with altitude. This effect is especially serious in scintillation measurement using the whole solar or lunar disk. In our MASP, we use a small subfield with a size of $5'' \times 5''$ as a guide star to sense the slope of phase, which is on the same order with the isoplanatic angle and the averaging effect of expand of the sensor elements is not serious. In the S-DIMM+ simulation in Kellerer et al. (2012), this effect is well simulated, and the results show r_0 can be well sensed. On the other hand, since the higher turbulence layer is generally weaker and have larger r_0, at a distance of 30 km, the effective size of the subaperture $D_{\rm eff} = 0.8$ m is comparable with the r_0 at high altitude. Thus this "cone effect" is not an obstacle for the MASP.

7. CONCLUSIONS

In this article, we introduced the concept of a multiple-aperture seeing profiler (MASP), which used two small telescopes instead of a large aperture. In the S-DIMM+ seeing retrieving approach, the maximum height is related with the size of diameter of the telescope and the separation of the subfields. Increasing the diameter of the telescope will lead to higher maximum detection altitude. However, for a new site-seeing test, a big telescope will not be available, while for a well-developed site with a large telescope, the observation time is very limited. Thus, accurate measurement of the multilayer seeing profile is difficult. Our MASP, which uses two portable small telescopes, is designed to solve this problem.

One of the obstacles for MASP is that the subaperture combination distances are not continuous, which will result in the information loss of corresponding height of atmosphere layers. We found that carefully choosing subapertures can provide the missing subaperture distances and thus recover the corresponding information. We used numerical simulation to evaluate the performance of MASP. The results indicate that the MASP using two 400-mm telescopes can deliver similar performance to a large telescope with 1120 mm aperture. For a single-layer case,

This content downloaded from 130.166.194.113 on Fri, 2 Oct 2015 17:06:50 PM
All use subject to JSTOR Terms and Conditions

the MASP delivers a retrieving seeing parameter with 5% estimated rms error, with a maxima measurement height up to 29 km.

For a multilayer seeing profile, we can also retrieve the strengths of each turbulence layers. We numerically simulated atmospheric profiles with four layers, and using 11 layers to sample the profile. The results show that all of the four layers can be well measured, with error less than 6%.

Both the simulations of single layer and multilayer show that our MASP works well, and can retrieve the multilayer profile with error of ∼5%. If one wants to improve the accuracy or using more layers to sample the profile, several methods exist, including using more subfields as well as using more short-exposure images.

We are grateful to Dr. Aglae Kellerer for helpful suggestions on atmospheric structure functions. This work is supported by Mt. Cuba Astronomical Foundation, National Science Foundation (NSF) under the grant ATM-084144, and partially supported by the National Natural Science Foundation of China (NSFC) under the grants 11220101001, 11433007, 11328302, 11373005, and 11303064, CAS special funding KT2013-10022, the Strategic Priority Research Program of the Chinese Academy of Sciences (Grant No. XDA04075200 and XDA04070600), the special funding for Young Researcher of Nanjing Institute of Astronomical Optics & Technology, as well as the Open Project of Key Laboratory of Astronomical Optics & Technology.

REFERENCES

Aristidi, E., Fossat, E., Agabi, A., et al. 2009, A&A, 499, 955
Avila, R., Avilés, J. L., Wilson, R. W., et al. 2008, MNRAS, 387, 1511
Avila, R. 2012, in Topics in Adaptive Optics, ed. K. T. Robert (Croatia: INTECH, 3
Bally, J., Theil, D., Billawalla, Y., et al. 1996, PASA, 13, 22
Beckers, J. M. 1993, Sol. Phys., 145, 399
———. 2001, Exp. Astron., 12, 1
Beckers, J. 2002, Astronomical Site Evaluation in the Visible and Radio Range, 266, 350
Berkefeld, T., & Soltau, D. 2010, Astron. Nachr., 331, 640
Boccas, M., Rigaut, F., Gratadour, D., et al. 2008, Proc. SPIE, 7015, 70150 X
Britton, M. C. 2006, PASP, 118, 885
Butterley, T., Wilson, R. W., & Sarazin, M. 2006, MNRAS, 369, 835
Egner, S. E., & Masciadri, E. 2007, PASP, 119, 1441
Fusco, T., Conan, J.-M., Mugnier, L. M., Michau, V., & Rousset, G. 2000, A&AS, 142, 149
Goodwin, M., Jenkins, C., & Lambert, A. 2007, Opt. Exp., 15, 14844
Hill, F., Beckers, J., Brandt, P., et al. 2006, Proc. SPIE, 6267, 62671 T
Johansson, E. M., & Gavel, D. T. 1994, Proc. SPIE, 2200, 372
Kellerer, A., Gorceix, N., Marino, J., Cao, W., & Goode, P.R. 2012, A&A, 542, AA 2
Kellerer, A. 2015, arXiv:physics.data-an/1504.00320
Milton, N. M., Lloyd-Hart, M., Bernier, J. A., & Baranec, C. 2007, Proc. SPIE, 6691, 66910 B
Myers, R. M., Hubert, Z., Morris, T. J., et al. 2008, Proc. SPIE, 7015, 70150 E
Okita, H., Ichikawa, T., Ashley, M. C. B., Takato, N., & Motoyama, H. 2013, A&A, 554, LL 5
Ren, D., Zhu, Y., Zhang, X., Dou, J., & Zhao, G. 2014, Appl. Opt., 53, 1683
Rimmele, T. R., & Marino, J. 2011, Living Reviews in Solar Physics, 8, 2
Rousset, G., Lacombe, F., Puget, P., et al. 2003, Proc. SPIE, 4839, 140
Sarazin, M., & Roddier, F. 1990, A&A, 227, 294
Scharmer, G. B., & van Werkhoven, T. I. M. 2010, A&A, 513, AA 25
Schmidt, D., Gorceix, N., Zhang, X., et al. 2014, Proc. SPIE, 9148, 91482 U
Seykora, E. J. 1993, Sol. Phys., 145, 389
Tokovinin, A. 2004, PASP, 116, 941
Tokovinin, A., Kornilov, V., Shatsky, N., & Voziakova, O. 2003, MNRAS, 343, 891
Tokovinin, A., & Travouillon, T. 2006, MNRAS, 365, 1235
Tokovinin, A., & Viard, E. 2001, Journal of the Optical Society of America A, 18, 873
Travouillon, T., Ashley, M. C. B., Burton, M. G., et al. 2003, A&A, 409, 1169
van Dam, M. A., Sasiela, R. J., Bouchez, A. H., et al. 2006, Proc. SPIE, 6272, 627231
Vernin, J., & Munoz-Tunon, C. 1994, A&A, 284, 311
Wang, L., Schöck, M., & Chanan, G. 2008, Appl. Opt., 47, 1880
Welsh, B. M. 1992, Appl. Opt., 31, 7283
Wildi, F. P., Brusa, G., Lloyd-Hart, M., Close, L. M., & Riccardi, A. 2003, Proc. SPIE, 5169, 17
Wilson, R. W. 2002, MNRAS, 337, 103
Wilson, R. W., Bate, J., Guerra, J. C., et al. 2004, Proc. SPIE, 5490, 758
Wilson, R.W., Butterley, T., & Sarazin, M. 2009, MNRAS, 399, 2129
Wilson, R. W., & Jenkins, C. R. 1996, MNRAS, 278, 39
Zhong, L., & Beckers, J. M. 2001, Sol. Phys., 198, 197

This content downloaded from 130.166.194.113 on Fri, 2 Oct 2015 17:06:50 PM
All use subject to JSTOR Terms and Conditions